Modelling of air-seawater interaction in marine electromagnetics

LEIF ABRAHAMSSON

FOI, Swedish Defence Research Agency, is a mainly assignment-funded agency under the Ministry of Defence. The core activities are research, method and technology development, as well as studies conducted in the interests of Swedish defence and the safety and security of society. The organisation employs approximately 1000 personnel of whom about 800 are scientists. This makes FOI Sweden's largest research institute. FOI gives its customers access to leading-edge expertise in a large number of fields such as security policy studies, defence and security related analyses, the assessment of various types of threat, systems for control and management of crises, protection against and management of hazardous substances, IT security and the potential offered by new sensors.

FOI
Defence Research Agency
Defence & Security,
Systems and Technology
SE-164 90 Stockholm

Phone: +46 8 555 030 00
Fax: +46 8 555 031 00

www.foi.se

FOI-R--3258--SE Technical report
ISSN 1650-1942 September 2011

Defence & Security, Systems and Technology

Leif Abrahamsson

Modelling of air-seawater interaction in marine electromagnetics

Titel	Modellering av koppling mellan luft och havsvatten i marin elektromagnetik
Title	Modelling of the air-seawater interaction in marine electromagnetics

Rapportnr/Report no	FOI-R--3258--SE
Rapporttyp Report Type	Teknisk rapport Technical Report
Sidor/Pages	30 p
Månad/Month	September
Utgivningsår/Year	2011
ISSN	ISSN 1650-1942
Kund/Customer	Försvarsmakten
Projektnr/Project no	E20684
Godkänd av/Approved by	Nils Olsson

FOI, Totalförsvarets Forskningsinstitut
Avdelningen för Försvars- och säkerhetssystem
164 90 Stockholm

FOI, Swedish Defence Research Agency
Division of Defence & Security, Systems and Technology
SE-164 90 Stockholm

Sammanfattning

Lågfrekventa elektromagnetiska fält i havsmiljöer är ett kunskapsområde av stor betydelse för det marina försvaret i tillämpningar som avmagnetisering, mindetektion och elektriska och magnetiska signaturer vid spaning. I denna rapport avhandlas matematiska och numeriska modeller för elektromagnetisk vågutbredning i gränsytan luft-havsvatten för elektriska och magnetiska källor och sensorer i vattenvolymen. Dessa modeller är hjälpmedel för utveckling och analys av system för spaning och skydd av marina enheter.

Elektromagnetiska lateralvågor som utbreder sig längs havsytan är ett fenomen av stor betydelse i marin elektromagnetik. Gångvägen löper från en ytnära källa i vattnet rakt upp till havsytan, där vågen utbreder sig i luften med ljushastigheten samtidigt som den exiterar vågor i vattnet genom bestrålning av vattenytan. Passagen i luftrummet gör att amplituden avtar mindre än gångvägar i vattnet och man får därmed längre utbredningsavstånd.

En viktig uppgift är att ta fram beräkningsmodeller för kvantifiering av faktiska amplituder i realistiska havsmiljöer med öar och stränder. I den här rapporten avhandlas speciellt finita differensmetoder eftersom de kan tillämpas i komplexa geometrier i 3D. För numeriska simuleringar av lateralvågen måste beräkningsområdet omfatta både luft och vatten vilket är problematiskt p.g.a. den enorma skillnaden i utbredningshastighet, som i sin tur medför helt vitt skilda krav på upplösning i rum och tid.

I den här rapporten ges en översikt av karakteristiska egenskaper hos lateralvågen som är relevanta för utveckling av numeriska modeller baserade på finita differenser. Särskild uppmärksamhet ägnas åt problemet med att avgränsa beräkningsområdet i luftrummet. Huvudresultatet är att höjden av luftskiktet måste vara ungefär tre gånger så stort som avståndet mellan sändare och mottagare för att lateralvågen ska kunna beräknas med god noggrannhet. Framtagna resultat illustreras med körexempel.

Nyckelord: lateralvåg, marin elektromagnetik, lågfrekvent, finit differensmetod, områdestrunkering

Summary

Low-frequency electromagnetic fields in sea environments are a topic of great importance in naval applications like degaussing, mine detection and surveillance. This report deals with mathematical and numerical models for electromagnetic wave propagation at the air-sea surface interface with electric and magnetic sources and receivers in seawater. These models provide tools for the development and analysis of systems of surveillance and protection in naval defence.

The lateral wave at the air/sea surface is a significant phenomenon at low frequency electromagnetic wave propagation in seawater. This wave takes a path that goes straight up to the sea surface from a submerged source in seawater, and then the wave propagates radially in air at speed of light and at the same time it induces waves in the seawater by reradiation. Amplitude decay during the propagation path in air is less than for paths in seawater, which makes it possible to achieve longer propagation distances than for a wave entirely confined in the water volume.

It is of great importance to develop computational models which are able to quantify actual amplitudes in realistic sea environments with islands and coast lines. In this work we are particularly interested in finite-difference methods because of their wide applicability. The inclusion of both air and seawater in the computational domain is a challenge because of the presence of vastly different wave speeds in air and seawater, which in turn induces different requirements on resolution in space and time.

In this report we review those characteristics of the lateral wave that are relevant for numerical modelling by a finite difference method. Special attention is devoted to the problem of domain truncation in the air space. Our main result is that the height of the air layer that needs to be included in the computational domain must be roughly equal to the triple of the source-receiver offset in order to reproduce the lateral wave with good accuracy.

Keywords: lateral wave, marine electromagnetics, low frequency, finite difference method, domain truncation

Contents

1 Introduction

Since World War II naval electromagnetics has been of great concern in applications like ASW, MCM, surveillance and communication. Until recently the design and optimisation of operational systems have relied on empirical knowledge. However in the past few decades mathematical modelling and computational techniques have become powerful complementary tools for analysis and performance predictions of systems in naval applications. At FOI considerable work is spent on the development and use of modelling tools. This report deals with a very specfic topic in modelling, namely the impact of the sea surface on low-frequency electromagnetic fields generated by sources in seawater. The approach of this work is to review basic theory of air-sea surface interaction in electromagnetics and pinpoint aspects that are useful for numerical modelling, in particular finite difference models.

The sea surface represents an abrupt change in impedance in electromagnetic wave propagation with a transmitter and receiver submerged in seawater. The impedance contrast increases at decreasing frequencies of a time-harmonic source. At 300 kHz the impedance ratio seawater/air is around 100, while it is infinite in the limit of vanishing frequency (DC). Yet a transmitter in seawater not too far from the sea surface in terms of skin depths (skin depth is ≈ 1 m at 300 kHz), will excite radiation into the air space. At low frequencies the radiation is guided along the sea surface, where the air wave radiates back in to the sea over distances which are long compared to those that can be achieved of a freely propagating wave in seawater. This is made possible by a propagation path that goes straight from the transmitter up to the sea surface, and then continues along sea surface in air, and then it turns straight down to subsurface receivers. This is the air-sea surface lateral wave, also termed the "up-over-down" mode of propagation. This wave suffers from dissipation at an exponential rate by distance in seawater, while the wave in air is subject to a lesser amplitude decay by geometrical spreading to some power (1-5) of the inverse of propagation distance.

The lateral wave is a fascinating phenomenon from physical, mathematical, numerical and application viewpoints. Physically it represents interaction of two physical processes, both of which are embodied by Maxwell's equations, diffusion in seawater and travelling waves in air. Mathematically the lateral wave is explained by the impact of a square-root singularity of a highly oscillatory integrand of an integral of plane wave solutions in a spectral decomposition of the radiated field. In numerical modelling of air-sea surface interaction by the FDTD (finite-difference time-domain) method with explicit time stepping, the time step must be adapted to the short time (speed of light) phenomena that takes place in the air space. Performing computations on such a small time scale is not realistic in view of the the much slower time scale of interest for the propagation in seawater (speed ≈ 100 km/s). One approach to overcome this problem is to truncate the computational domain at the sea surface by applying a boundary condition that accounts for the response of the air space. Another approach is to use implicit time stepping, or turn to computations in the frequency domain by the FDFD (finite-difference frequency-domain) method. In both cases a finite layer of air is included in the computational domain. The thickness of this layer must be large enough to ensure proper modelling of the lateral wave effect. At the same time the air layer

should be kept as small as possible to save computer time. To be able to decide on proper extent and necessary resolution of the computational grid, the characteristics of the air wave need to be known. For the most part available knowledge is provided by analytic expressions which describes how lateral waves depend on frequency regime and propagation distance. Those expressions are often of asymptotic form and subject to assumptions which are difficult to assess in a specific application. For this reason we intend to complement analytic approximations with numerical evaluations of solutions to the full problem. For the numerical calculations we use the software tools NLAYER [1] and the FDTD code [2].

A similar lateral wave appears at the seawater/seabed interface and at subbottom interfaces [3]. This lateral wave is known as the "down-under -up" mode of propagation. Its properties depend on the the conductivity contrast at the interface. This aspect deserves an investigation of its own, as well as the interaction between surface and seabed lateral waves in waters of finite depth.

In this report we restrict attention to a frequency range which coarsely extends from DC to 300 kHz. The frequency range of interest in marine electromagnetics is usually much lower. However the bound 300 kHz satifies two prerequisites in the theory of lateral waves in the low frequency regime. Namely near-field effects are predominant for propagation in air at short range ($\approx$ 1 km), while wave propagation in seawater is largely diffusive. The latter property implies that the concept of skin depth is relevant (skin depth is $\approx$ 1 m at 300 kHz).

The lateral wave is a concern in marine controlled-source electromagnetic surveys for hydrocarbon-saturated reservoirs [4]. It is especially problematic at shallow-water depths ($<$ 300 m) and at long offsets, where the lateral wave might mask the weak signal from a target at large depth ($\approx$ 1 km).

This paper is organized as follows. Sec. 2 is a review of plane wave reflection and transmission at the air-sea surface in the case of plane wave incidence from seawater. Well-known lateral-wave formulas for dipole sources are presented in Sec. 3. Sec. 4 is a review of the main characteristics of the field in air generated by a dipole source in seawater. In Sec. 5 we address the problem of truncating the air space in a lean way without compromising the accuracy of the lateral wave. In addition theoretical results are supported by computational examples which demonstrate the potential capability of finite difference modelling of lateral-wave propagation. The main conclusions of this work is found in Sec. 6.

2 Plane wave reflection at the air-seawater surface

The mathematical description of reflection and transmission of plane waves at the air-seawater surface is both simple and informative. The starting point of a plane wave analysis is Maxwell's equations

$$\begin{aligned} \nabla \times \mathbf{E} &= -\sigma^* H - \mu \tfrac{\partial \mathbf{H}}{\partial t}, \\ \nabla \times \mathbf{H} &= \sigma \mathbf{E} + \epsilon \tfrac{\partial \mathbf{E}}{\partial t}, \end{aligned} \tag{2.1}$$

for isotropic constitutive relations

$$\mathbf{D} = \epsilon\mathbf{E}, \quad \mathbf{B} = \mu\mathbf{H}.$$

The introduction of a fictitious magnetic conductivity σ_n^*, which is always set to zero, makes it easier to apply duality arguments for exchange of analytic expressions for solutions to electric and magnetic sources.

Attention is restricted to two half-spaces of air and seawater with a horizontal interface at $z = 0$ in a right handed coordinate system with the z-axis pointing downward. The half-spaces of air and seawater are also referred to as layer 1 respectively layer 2 and corresponding field components and media parameters are subscripted accordingly. Unless otherwise stated the media parameters for air and seawater are given by

air	**seawater**	
$\epsilon_1 = 8.854 \cdot 10^{-12}$	$\epsilon_2 = 81\epsilon_1,$	[As/Vm (or F/m)]
$\mu_1 = 4\pi 10^{-7}$	$\mu_2 = 4\pi 10^{-7},$	[Vs/Am (or H/m)]
$\sigma_1 = 0$	$\sigma_2 = 0.8,$	[A/Vm (or S/m)]

The notation μ without subscript is also used, since both media are nonmagnetic.

As usual the description of plane wave reflection is done in the vertical plane $y = 0$ (plane of incidence), while all field components are constant in the y-direction. The time dependence is assumed to be of the form $e^{-i\omega t}$, $\omega = 2\pi f$, f= frequency in Hz. By the substitutions

$$\frac{\partial}{\partial t} \leftrightarrow -i\omega \quad \text{and} \quad \frac{\partial}{\partial y} = 0$$

Maxwell's equations decouple into two separate systems, the TE-case with

$$\begin{aligned} &E_y, H_x, H_z \text{ as unkowns, while} \\ &E_x = E_z = H_y = 0 \end{aligned} \tag{2.2}$$

and the TM-case with

$$\begin{aligned} &H_y, E_x, E_z \text{ as unkowns, while} \\ &E_y = H_x = H_z = 0. \end{aligned} \tag{2.3}$$

The systems for the TE-case has the form

$$\begin{aligned} (\sigma - i\omega\epsilon)E_y &= \tfrac{\partial H_x}{\partial z} - \tfrac{\partial H_z}{\partial x} \\ -(\sigma^* - i\omega\mu)H_x &= -\tfrac{\partial E_y}{\partial z} \\ -(\sigma^* - i\omega\mu)H_z &= \tfrac{\partial E_y}{\partial x} \end{aligned} \tag{2.4}$$

which can be written as a single equation of second order equation for E_y:

$$\frac{\partial}{\partial x}\left(\frac{1}{-(\sigma^* - i\omega\mu)}\frac{\partial E_y}{\partial x}\right) + \frac{\partial}{\partial z}\left(\frac{1}{-(\sigma^* - i\omega\mu)}\frac{\partial E_y}{\partial z}\right) + (\sigma - i\omega\epsilon)E_y = 0. \tag{2.5}$$

In the TM-case the corresponding system reads

$$\begin{aligned} -(\sigma^* - i\omega\mu)H_y &= \tfrac{\partial E_x}{\partial z} - \tfrac{\partial E_z}{\partial x} \\ (\sigma - i\omega\epsilon)E_x &= -\tfrac{\partial H_y}{\partial z} \\ (\sigma - i\omega\epsilon)E_z &= \tfrac{\partial H_y}{\partial x} \end{aligned} \tag{2.6}$$

which can be reformulated as single equation for H_y:

$$\frac{\partial}{\partial x}\left(\frac{1}{\sigma - i\omega\epsilon}\frac{\partial H_y}{\partial x}\right) + \frac{\partial}{\partial z}\left(\frac{1}{\sigma - i\omega\epsilon}\frac{\partial H_y}{\partial z}\right) - (\sigma^* - i\omega\mu)H_y = 0. \tag{2.7}$$

In each case there is one system for air and another one for seawater. The solutions to these systems are constrained at the air-sea surface interface by the continuity of tangential electric and magnetic fields. For the TE-case it implies that

$$E_y, H_x \quad \left(\text{or equivalently } E_y, \frac{1}{\mu}\frac{\partial E_y}{\partial z}\right) \tag{2.8}$$

are continuous at $z = 0$, while the continuity of

$$H_y, E_x \quad \left(\text{or equivalently } H_y, \frac{1}{\sigma - i\omega\epsilon}\frac{\partial H_y}{\partial z}\right) \tag{2.9}$$

holds in the TM case.

2.1 Reflection and transmission coefficients

Next consider an incoming E_y^I plane wave solution from seawater, which is decomposed at the air-sea surface into a reflected component E_y^R and a transmitted wave E_y^T into the air space. The mathematical form of these solutions are

$$E_y^I = e^{ikx - ik_{2z}z}, \quad E_y^R = R^{TE}e^{ikx + ik_{2z}z}, \quad E_y^T = T^{TE}e^{ikx - ik_{1z}z}, \tag{2.10}$$

where the wave numbers are given by

$$\begin{aligned} &k_1^2 = -(\sigma_1^* - i\omega\mu_1)(\sigma_1 - i\omega\epsilon_1) = \omega^2\mu_1\epsilon_1, \\ &k_{1z} = \sqrt{k_1^2 - k_x^2}, \quad Imk_{1z} \geq 0, \\ &k_2^2 = -(\sigma_2^* - i\omega\mu_2)(\sigma_2 - i\omega\epsilon_2) = i\omega\mu_2\sigma_2 + \omega^2\mu_2\epsilon_2, \\ &k_{2z} = \sqrt{k_2^2 - k_x^2}, \quad Imk_{2z} \geq 0. \end{aligned} \tag{2.11}$$

The magnetic components, which are obtained from the equations (2.4) are given by

$$\begin{aligned} H_x^I + H_x^R &= \tfrac{ik_{2z}}{-(\sigma_2^* - i\omega\mu_2)}(e^{-ik_{2z}z} - R^{TE}e^{ik_{2z}z})e^{ikx} \\ H_x^T &= \tfrac{ik_{1z}}{-(\sigma_1^* - i\omega\mu_1)}T^{TE}e^{ikx - ik_{1z}z} \\ H_z^I + H_z^R &= \tfrac{ik_x}{-(\sigma_2^* - i\omega\mu_2)}(e^{-ik_{2z}z} + R^{TE}e^{ik_{2z}z})e^{ikx} \\ H_z^T &= \tfrac{ik_x}{-(\sigma_1^* - i\omega\mu_1)}T^{TE}e^{ikx - ik_{1z}z} \end{aligned} \tag{2.12}$$

The Poynting vector at the air-sea surface $z = 0$ is given by

$$\mathbf{P} = \frac{1}{2}Re(\mathbf{E} \times \mathbf{H}^*) = \frac{1}{2}Re(E_y H_z^* \hat{\mathbf{x}} - E_y H_x^* \hat{\mathbf{z}})$$

which on the aerial side assumes the form

$$\begin{aligned} P_x &= \tfrac{1}{2} Re\left\{ \tfrac{-ik_x}{-(\sigma_1^* - i\omega\mu_1)} \right\} |T^{TE}|^2 \\ P_z &= -\tfrac{1}{2} Re\left\{ \tfrac{-i\bar{k}_{1z}}{-(\sigma_1^* - i\omega\mu_1)} \right\} |T^{TE}|^2 \end{aligned} \tag{2.13}$$

for the plane wave solutions (2.10) and (2.12).

The reflection and transmission coefficients R^{TE} and T^{TE} are determined by the boundary conditions (2.8), which results in

$$R^{TE} = \tfrac{k_{2z} - k_{1z}}{k_{2z} + k_{1z}}, \quad T^{TE} = \tfrac{2k_{2z}}{k_{2z} + k_{1z}}. \tag{2.14}$$

The corresponding formulas for the TM case are given by

$$H_y^I = e^{ikx - ik_{2z}z}, \quad H_y^R = R^{TM} e^{ikx + ik_{2z}z}, \quad H_y^T = T^{TM} e^{ikx - ik_{1z}z}. \tag{2.15}$$

The electric components, which are obtained from the equations (2.6) are given by

$$\begin{aligned} E_x^I + E_x^R &= \tfrac{ik_{2z}}{\sigma_2 - i\omega\epsilon_2}(e^{-ik_{2z}z} - R^{TM} e^{ik_{2z}z}) e^{ikx} \\ E_x^T &= \tfrac{ik_{1z}}{\sigma_1 - i\omega\epsilon_1} T^{TM} e^{ikx - ik_{1z}z} \\ E_z^I + E_z^R &= \tfrac{ik_x}{\sigma_2 - i\omega\epsilon_2}(e^{-ik_{2z}z} + R^{TM} e^{ik_{2z}z}) e^{ikx} \\ E_z^T &= \tfrac{ik_x}{\sigma_1^* - i\omega\epsilon_1)} T^{TM} e^{ikx - ik_{1z}z} \end{aligned} \tag{2.16}$$

The Poynting vector at the air-sea surface is given by

$$\mathbf{P} = \frac{1}{2} Re(\mathbf{E} \times \mathbf{H}^*) = \frac{1}{2} Re(-E_z H_y^* \hat{\mathbf{x}} + E_x H_y^* \hat{\mathbf{z}})$$

which on the aerial side assumes the form

$$\begin{aligned} P_x &= -\tfrac{1}{2} Re\left\{ \tfrac{ik_x}{\sigma_1 - i\omega\epsilon_1)} \right\} |T^{TM}|^2 \\ P_z &= \tfrac{1}{2} Re\left\{ \tfrac{-i\bar{k}_{1z}}{\sigma_1 - i\omega\epsilon_1} \right\} |T^{TM}|^2. \end{aligned} \tag{2.17}$$

for the the plane wave solutions (2.15) and (2.16).

By imposing the boundary conditions the reflection and transmission coefficents are determined by

$$R^{TM} = \tfrac{k_{2z}k_1^2 - k_{1z}k_2^2}{k_{2z}k_1^2 + k_{1z}k_2^2}, \quad T^{TM} = \tfrac{2k_{2z}k_1^2}{k_{2z}k_1^2 + k_{1z}k_2^2}. \tag{2.18}$$

2.2 Analysis of the reflection coefficient

For a plane wave with normal incidence towards the sea surface

$$k_x = 0, \qquad k_{1z} = k_1, \qquad k_{2z} = k_2,$$

the reflection and transmission coefficients (2.14) and (2.18) are given by

$$\begin{aligned} R^{TE} &= \frac{1-\frac{k_1}{k_2}}{1+\frac{k_1}{k_2}}, & T^{TE} &= \frac{2}{1+\frac{k_1}{k_2}}, \\ R^{TM} &= -\frac{1-\frac{k_1}{k_2}}{1+\frac{k_1}{k_2}}, & T^{TM} &= \frac{2\frac{k_1}{k_2}}{1+\frac{k_1}{k_2}}. \end{aligned} \tag{2.19}$$

The deviation of the ratio k_1/k_2 from unity is a measure of the impedance contrast between air and seawater, since

$$\begin{aligned} Z_1^{TE} &= -\frac{E_y}{H_x} = \frac{\omega\mu}{k_1}, & Z_2^{TE} &= \frac{\omega\mu}{k_2}, \\ Z_1^{TM} &= \frac{E_x}{H_y} = \frac{k_1}{\omega\epsilon_1}, & Z_2^{TM} &= \frac{-ik_2}{\sigma_2 - i\omega\epsilon_2}. \end{aligned} \tag{2.20}$$

In both cases it can be verified that k_1/k_2 equals Z_2/Z_1. Figure 2.1 depicts how the impedance ratio depends on frequencies from 0.1 Hz to 1 GHz. We note that

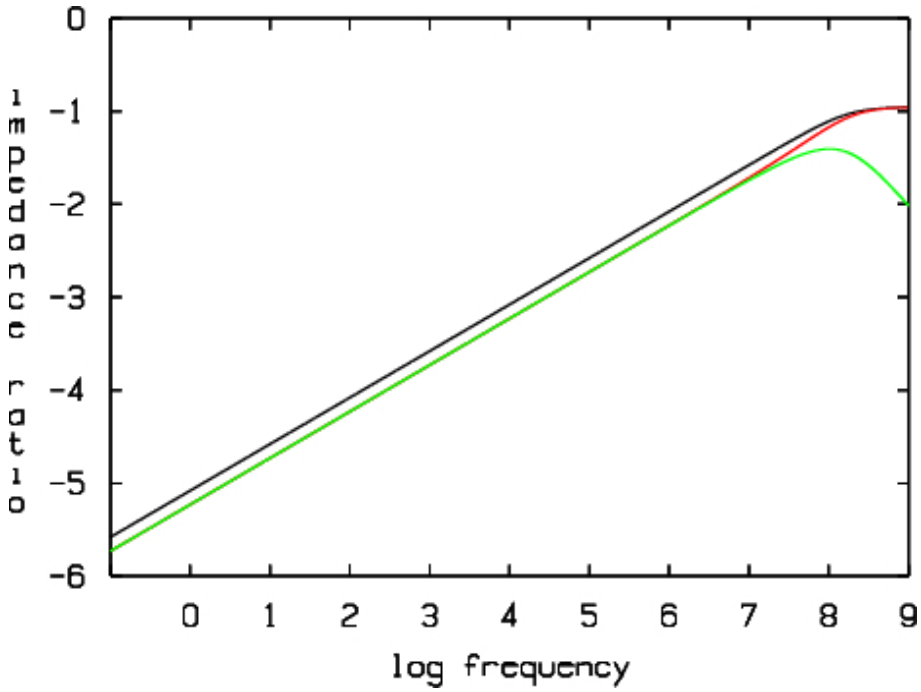

Figure 2.1: *The magnitude of the ratio of wavenumbers k_1/k_2 (black) of air and seawater as function of frequency with both axes in log_{10}-scale. The absolute values of real and the imaginary parts of the wavenumber ratio are plotted in red respectively green lines.*

the impedance contrast diminishes at increasing frequencies. Somewhat arbitrarily we restrict attention to frequencies less than 300 kHz. At the frequency 300 kHz we obtain

$$k_1 = 2\pi 10^{-3}, \quad k_2 = (0.974, 0.973), \quad |\tfrac{k_1}{k_2}| = 4.57 \cdot 10^{-3} \quad \text{(f=300 kHz)}. \tag{2.21}$$

The wavenumber in air is commonly expressed in terms of wavelength λ_1 by means of the relationship $k_1 = 2\pi/\lambda_1$. At the frequency 300 kHz the wavelength is λ_1= 1 km. In seawater propagation constants are rather expressed in terms of skin depth and Q-factor. The Q-factor is the the ratio of displacement and conduction currents, $Q = \omega\epsilon_2/\sigma_2$, which at the frequency 300 kHz yields Q= 0.0017. Thus even at this high frequency wave propagation in seawater is predominantly diffusive. When displacement currents are neglected the wavenumber (2.11) for k_2 in seawater is often written in the form

$$k_2 = (1+i)\delta^{-1}, \quad \delta = \sqrt{\tfrac{2}{\omega\mu\sigma_2}}, \tag{2.22}$$

where δ is the skin depth. At the frequency 300 kHz, δ=1.03 m, which means that propagation range is on the order of a few meters as field amplitudes decay by a factor e^{-1} per skin depth.

The ratio of wavenumbers k_1/k_2 serves as a perturbation parameter in approximate formulas of low-frequency propagation in air-sea environments. For example the reflection and transmission coefficients (2.19) for normal incidence may be approximated by

$$\begin{array}{ll} R^{TE} \approx 1, & T^{TE} \approx 2, \\ R^{TM} \approx -1, & T^{TM} \approx 2\frac{k_1}{k_2}. \end{array} \tag{2.23}$$

This approximation improves by decreasing frequency and in the limit of vanishing frequency (DC) it is exact. The possible proximity to the DC-case is of particular importance for modelling. In the finite difference method for DC fields in seawater the influence of the sea surface is modelled by the boundary condition of vanishing normal component of the E-field ($E_{2z} = 0$). It implies that the computational domain can be truncated at the sea surface. For AC problems this boundary condition would correspond to setting tangential H-fields equal to zero. However this boundary condition is perfectly reflecting and there would be no energy transfer to air space. From the z-component of the Poynting vectors (2.13) and (2.17) we see that radiation into the air space takes place for horizontal wavenumbers k_x in the range $[0, k_1)$. Since $k_1 << |k_2|$, the leakage of energy is confined to wave directions very close to the normal, while total reflection prevails elsewhere. The ratio of incident and transmitted energy fluxes in the TE-case is given by

$$\frac{P_z^T}{P_z^I} = \frac{Re\left\{\bar{k}_{1z}\right\}|T^{TE}|^2}{Re\left\{\bar{k}_{2z}\right\}} = \begin{cases} \approx \frac{4\sqrt{k_1^2-k_x^2}}{|Re\left\{\bar{k}_{2z}\right\}|}, & 0 \le k_x < k_1 \\ 0, & k_x \ge k_1. \end{cases} \tag{2.24}$$

We note that the ratio of energy fluxes is of the order $|k_1/k_2|$. In the TM case the expression for energy tranfer is more complicated because the reflection and transmission coefficients undergo large transitions around $k_{1z} = 0$. Figure 2.2 shows a numerical evaluation of the ratio of transmitted and incident vertical energy fluxes over the entire radiation range $[0, k_1)$ of k_x for both TE and TM cases at the frequency 1 kHz.

We note that the flux curves start to part beyond $k_x = 0$ and when $k_x \approx k_1$ radiation in the TM case is enhanced as opposed to the TE-case. It imples that transmitted wave energy propagates preferentially in the horizontal direction in the TM case.

Figure 2.3 shows the reflection coefficients R^{TE} and R^{TM} in a horizontal wavenumber interval $[0, 2Rek_2]$, which is relevant for propagation in seawater.

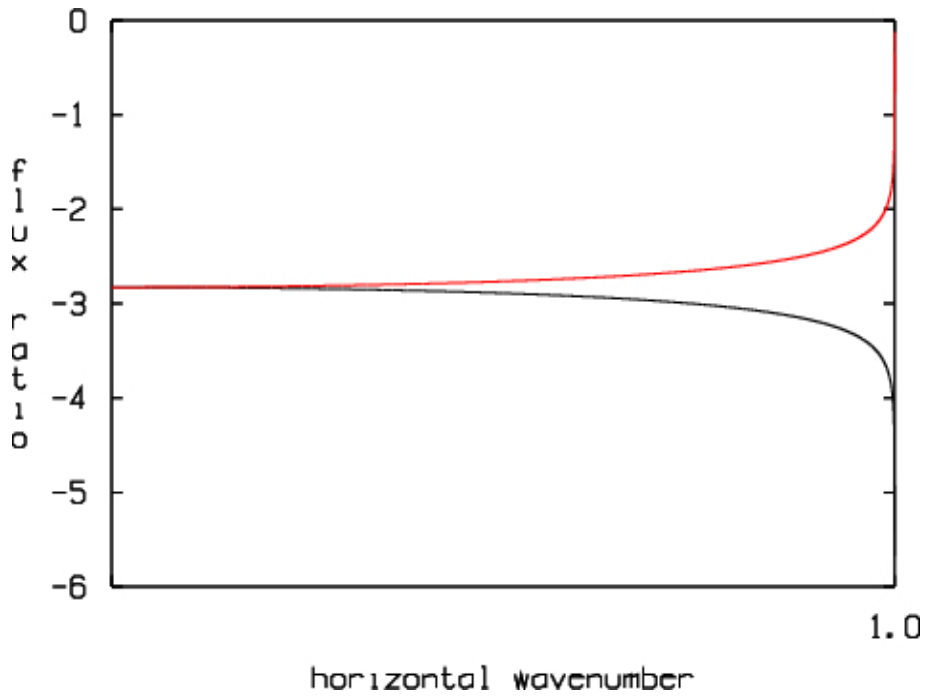

Figure 2.2: *The the ratio (in $\log_{10}$-scale) of transmitted and incident vertical components of the Poynting vectors in the TE-case (black) and TM-case (red) as function of normalized horizontal wavenumber k_x/k_1 in the radiation interval $0 \leq k_x < k_1$. The frequency is 1 kHz.*

We see that R^{TM} is almost identical to the DC case $R^{TM} = -1$, while there is a clear departure of R^{TE} from the DC case $R^{TE} = 1$. This behavior can be verfied analytically as follows

$$\begin{aligned} R^{TE} - 1 = \; & \tfrac{k_{2z}-k_{1z}}{k_{2z}+k_{1z}} - 1 = -2\tfrac{k_{1z}}{k_{2z}+k_{1z}} = -2\tfrac{k_{1z}(k_{2z}-k_{1z})}{k_2^2-k_1^2} = \\ & -2\tfrac{k_{1z}k_{2z}-k_1^2+k_x^2}{k_2^2-k_1^2} \approx -2\tfrac{ik_xk_{2z}+k_x^2}{k_2^2} \\ R^{TM} + 1 = \; & \tfrac{k_{2z}k_1^2-k_{1z}k_2^2}{k_{2z}k_1^2+k_{1z}k_2^2} + 1 = 2\tfrac{k_{2z}k_1^2}{k_{2z}k_1^2+k_{1z}k_2^2} \approx 2\tfrac{k_{2z}}{ik_x}\tfrac{k_1^2}{k_2^2}. \end{aligned} \tag{2.25}$$

The approximate expressions were arrived at by using $|k_1/k_2| << 1$ and the condition that $k_x > k_1$. The above estimates show that $|R^{TM}+1|$ is small, while $|R^{TE}-1|$ is far from being zero.

Plane wave decomposition is used to derive solutions to wave propagation problems with sources of finite spatial extent. Then the solution is expressed as an integral of plane wave solutions, in which the singularites of the reflection coefficients have a profound influence of the nature of the solution. For the reflection coefficients (2.14) and (2.18) there are square-root singularities of k_{1z} at k_1 and k_{2z} at k_2. The former one is of particular interest because it governs the interaction with the air space. From the expressions (2.25)

$$\begin{aligned} & R^{TE} - 1 = -2\tfrac{k_{1z}}{k_{2z}+k_{1z}} = -2\tfrac{k_{1z}(k_{2z}-k_{1z})}{k_2^2-k_1^2} = -2\tfrac{(k_{1z}k_{2z}-k_1^2+k_x^2)}{k_2^2-k_1^2} \\ & R^{TM} + 1 = 2\tfrac{k_{2z}k_1^2}{k_{2z}k_1^2+k_{1z}k_2^2} \end{aligned} \tag{2.26}$$

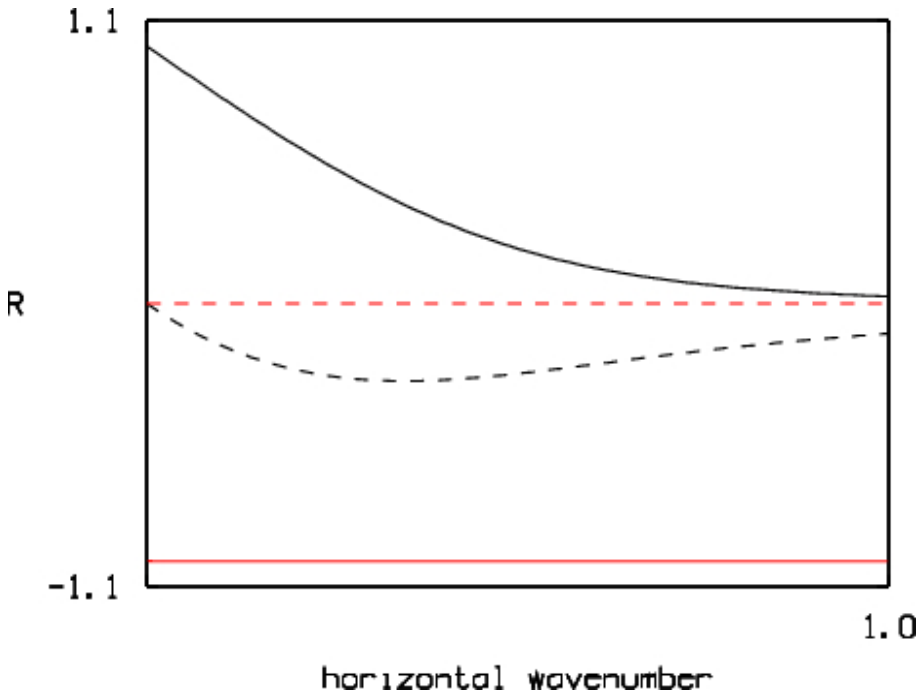

Figure 2.3: *The real (solid lines) and imaginary part (dashed lines) of the reflection coefficient in the TE-case (black) and TM-case (red) as function of normalized horizontal wavenumber $k_x/2Rek_2$ for horizontal wavenumbers in the range $0 \leq k_x \leq 2Rek_2$. The frequency is 1 kHz.*

we see that the singularity around $k_x \approx k_1$ is of the form

$$R^{TE} \sim -2\frac{k_{1z}}{k_2}, \quad R^{TM} \sim 2\frac{k_1^2}{k_2}\frac{1}{k_{1z}}. \tag{2.27}$$

The singularity in the TM case is stronger as it involves the inverse of the square-root $k_{1z} = \sqrt{k_1^2 - k_x}$. However it is counterbalanced by a multiplying factor k_1^2/k_2 which is very small at low frequencies.

The field of a low-frequency VED source in a horizontally layered environment has the characteristics of pure TM mode of propagation, and the lateral wave at the sea surface generated by a VED source is practically neglible. This fact has spurred interest in using VED sources in hydrocarbon surveys because it would eliminate the influence of the air wave [5]. However this is true only in a first approximation because the presence of scattering objects in a layered structure will cause deviations from the pure TM case. Therefore domain truncation at the sea surface by setting the horizontal magnetic field to zero at the sea surface would be feasible only in exceptional cases.

3 Lateral-wave formulas for dipole sources

The determination of electromagnetic (EM) fields from time-harmonic dipoles in horizontally layered media has a long history which dates back to 1909 when Sommerfeld presented the radiation field from a dipole above above a conductive half-space. In a cylindrical coordinate system (ρ, ϕ, z) with a vertical z-axis through the center of the

source the solution can be expressed in terms of integrals of the form

$$\begin{aligned} I(\rho,\phi,z_r,z_s) &= \int_0^\infty G(k,z_r,z_s,\phi)J_\nu(k\rho)kdk, \\ J_\nu &= \text{Bessel function of order } \nu, \quad \nu = 0,1, \\ G &= \text{spectral domain Green's function}, \\ \rho &= \text{radial source-receiver distance}, \\ \phi &= \text{azimuthal angle}, \\ z_s/z_r &= \text{source/receiver depths}. \end{aligned} \tag{3.1}$$

The Green's function represents the media response to incidence of plane waves with the radial wavenumber k and amplitudes determined by a plane-wave decomposition of the EM field from a dipole in a whole-space. An integral of the generic type (3.1) is commonly called the Sommerfeld integral.

For two half-spaces of air and seawater the Green's function in (3.1) can be expressed in analytic form. The book of King et al.[6] contains a thorough derivation and analysis of EM fields from VED and HED sources. It is shown that the solution is composed of four different parts. These are the direct field, the reflected field due to an ideal image source, the lateral-wave field and a correction term. The general form of the lateral-wave component is typified by the radial $E^L_{2\rho}$-field of an HED of unit strength (Idl= 1Am):

$$E^L_{2\rho} = \underbrace{\frac{\omega\mu}{2\pi}\frac{i\cos\phi}{k_2^2}\frac{1}{\rho^3}}_{G_L} \cdot \underbrace{e^{ik_2(z_s+z_r)}e^{ik_1\rho}}_{P_L} \tag{3.2}$$

The propagation factor P_L in (3.2) expresses the fact that the wave travels partly in seawater along vertical paths up and down and partly in air along the sea surface. Since the propagation constant k_1 in air is real, the last term of P_L represents a phase shift, which is neglible as $k_1\rho$ is extremely small for problems under this study. In the time-domain it would correspond to a time delay for traversing the radial distance ρ at the speed of light. The first factor of P_L accounts for two vertical paths in the seawater, one up to the sea surface at the source and another one down from the sea surface at the depth of the receiver. The loss factor along these paths amounts to $e^{-(z_s+z_r)/\delta}$, where δ is the skin depth (2.22). The geometric factor G_L expresses amplitude decay by radial distance due to geometrical spread. This factor may also include impact by frequency, directivity and media parameters. Table 3.1 is a tableau over G_L-factors of lateral waves generated by VED, VMD, HED and HMD sources. These formulas are approximations based on the assumptions:

$$|\tfrac{k_1}{k_2}| < 0.01, \quad \tfrac{\rho}{z_s} > 5, \quad \tfrac{\rho}{z_r} > 5. \tag{3.3}$$

We see that the geometrical spread factor assumes the form ρ^{-m}, m=2,..,5, depending on dipole type and field component. Those with the least spread ρ^{-2} also contain the factor $\frac{k_1}{k_2}$ squared, which means that their excitation is minute at low frequencies. For example this holds for all lateral-wave components of a VED. The field of a VED source consists of pure TM modes in a plane wave decomposition, for which the interaction at the sea surface is similar to DC. We also note that the lateral-wave field of

Table 3.1: *Geometric factors G_L of lateral waves for VED, VMD, HED and HMD sources and receivers located in seawater. The strength of electric and magnetic sources is set to Idl=1 Am respectively M= 1 Am^2.*

dipole type	geometric factor G_L of lateral waves $G_L \cdot P_L$ of type (3.2)					
	$E^L_{2\rho}$	$E^L_{2\phi}$	E^L_{2z}	$B^L_{2\rho}$	$B^L_{2\phi}$	B^L_{2z}
VED	$\frac{\omega\mu}{2\pi}\frac{k_1^2}{k_2^2}\frac{1}{\rho^2}$	0	$-\frac{\omega\mu}{2\pi}\frac{ik_1^2}{k_2^4}\frac{1}{\rho^3}$	0	$\frac{\mu}{2\pi}\frac{k_1^2}{k_2^2}\frac{1}{\rho^2}$	0
VMD	0	$-\frac{3\omega\mu}{2\pi}\frac{i}{k_2^2}\frac{1}{\rho^4}$	0	$\frac{3\mu}{2\pi}\frac{i}{k_2}\frac{1}{\rho^4}$	0	$\frac{9\mu}{2\pi}\frac{i}{k_2^2}\frac{1}{\rho^5}$
HED	$\frac{\omega\mu}{2\pi}\frac{i\cos\phi}{k_2^2}\frac{1}{\rho^3}$	$\frac{\omega\mu}{\pi}\frac{i}{k_2^2}\frac{\sin\phi}{\rho^3}$	$-\frac{\omega\mu}{2\pi}\frac{k_1^2}{k_2^3}\frac{\cos\phi}{\rho^2}$	$-\frac{\mu}{\pi}\frac{i}{k_2}\frac{\sin\phi}{\rho^3}$	$\frac{\mu}{2\pi}\frac{i}{k_2}\frac{\cos\phi}{\rho^3}$	$-\frac{3\mu}{2\pi}\frac{1}{k_2^2}\frac{\sin\phi}{\rho^4}$
HMD	$\frac{\omega\mu}{2\pi}\frac{1}{k_2}\frac{\sin\phi}{\rho^3}$	$-\frac{\omega\mu}{\pi}\frac{1}{k_2}\frac{\cos\phi}{\rho^3}$	$\frac{\omega\mu}{2\pi}\frac{ik_1^2}{k_2^2}\frac{\sin\phi}{\rho^2}$	$\frac{\mu}{\pi}\frac{\cos\phi}{\rho^3}$	$\frac{\mu}{2\pi}\frac{\sin\phi}{\rho^3}$	$-\frac{3\mu}{2\pi}\frac{i}{k_2}\frac{\cos\phi}{\rho^4}$

a VMD exhibits a geometrical spread like ρ^{-4} as compared to ρ^{-3} for that of a HED or HMD. The formulas in Table 3.1 are simpler than those for the direct field. Nevertheless comparisons with numerical evaluations of full field solutions show that the accuracy of lateral wave formulas is excellent for source and receivers within a few skin depths from the sea surface and at source-receiver off-sets larger than 5-10 skin depths. This is confirmed by two examples, which are not exceptional, shown in Figure 3.1. Here comparisons of exact solutions with those from lateral-wave formulas are made for HED and VMD sources at 1 kHz. The skin depth at 1 kHz is 17.8 m.

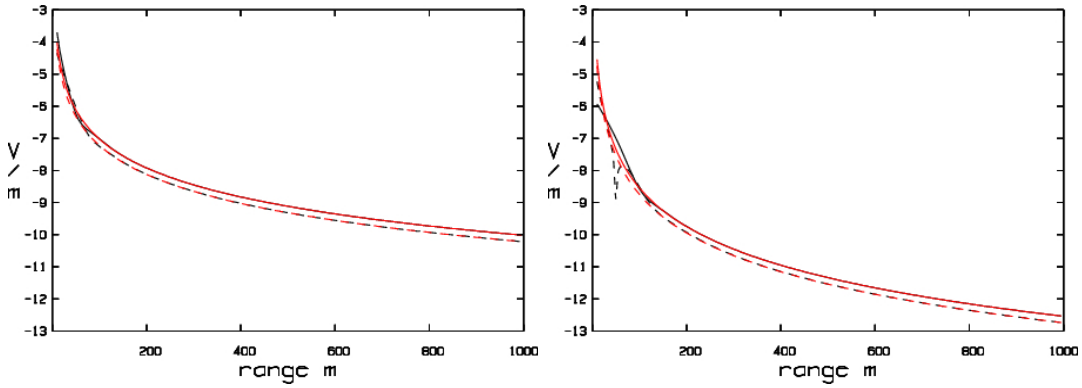

Figure 3.1: *Comparisons of exact solutions and those obtained by lateral wave formulas of the $E_{2\rho}$ component of an HED (left panel) and the $E_{2\phi}$ component of a VMD (right panel) for ϕ=0 as function of range. The real and imaginary parts of the full solutions are depicted in solid black respectively dased black lines, while lateral wave formulas are drawn in red colour. The source and receiver depths are both 5 m and the frequency is 1 kHz. The source strength is unity and the fields are shown in V/m in in log_{10}-scale.*

In Figure 3.1 solution curves are almost coincident beyond 100 m. We also note that the rate of decay is larger in the VMD case, ρ^{-4} versus ρ^{-3} for the HED.

A notable characteristic of the lateral wave is that some components are almost independent of frequency. For example, for an HED source

$$E^L_{2\rho} = \frac{\omega\mu}{2\pi}\frac{i\cos\phi}{k_2^2}\frac{1}{\rho^3}e^{ik_2(z_s+z_r)}e^{ik_1\rho} \approx \frac{1}{2\pi}\frac{\cos\phi}{\sigma_2}e^{ik_2(z_s+z_r)} \tag{3.4}$$

depends weakly on frequency in the case that source and receiver depths are shallow in terms of skin depth. This is illustrated in Figure 3.2, which shows propagation of a Ricker pulse with the center frequency 1 kHz over distances 100, 150 and 200 m both in the presence of a sea surface (left panel) and in a whole-space (right panel). In the

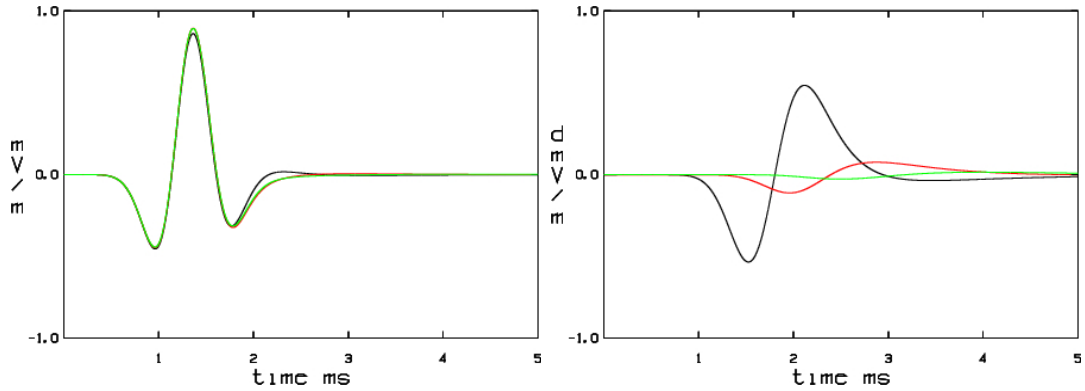

Figure 3.2: *Comparisons of E_{2x} components of HED transmissions of Ricker pulses with center frequency 1 kHz at the ranges 100 (black), 150 (red) and 200 m (green). The left panel shows responses in the presence of a sea surface while the right panel show solutions in a whole-space of seawater. In both cases the time series at 150 and 200 m have been multiplied by 1.5^3 respectively 2^3 to compensate for geometrical spread. The source and receiver depths are both 5 m and the source strength is 8 Am. The amplitudes are plotted in mV/m (left panel) and dmV/m (right panel).*

graphical presentations the time series of receivers at 150 and 250 m were multiplied by the factors 1.5^3 respectively 2^3 in order to enhance the significance of the expected decay rate ρ^{-3} by distance. As a result of this rescaling and the slight frequency dependence, the waveforms in the left panel are almost identical and equal to the waveform emitted at the source. In a whole-space (right panel) the same compensation for geometrical spread was applied but its effect cannot be noticed because the decay in seawater is exponential. Another notable difference is time of arrivals. The lateral wave arrives earlier because it travels the lateral distance in air at the speed of light.

4 The field in air of a dipole source in seawater

Knowledge of the electromagnetic field in air from a submerged dipole is helpful for development of an effective treatment of the air space in a finite-difference method. A detailed derivation and analysis of fields in the air from VED and HED sources is presented in [6]. The field in the air resembles radiation from a point source located at the sea surface on the aerial side. For a submerged HED part of the radiated field is analogous to a y-directed HMD with the source strength

$$M = \frac{2Idl}{ik_2} e^{ik_2 z_s}, \quad [\mathrm{Am}^2], \tag{4.1}$$

where Idl is the strength of the HED. For example, the $E_{1\rho}$ and $B_{1\phi}$ components in air from an HED source of unit strength in seawater has the appearance

$$
\begin{aligned}
E_{1\rho} &\approx \frac{\omega\mu}{2\pi}\frac{\cos\phi}{k_2}e^{ik_2 z_s}\left(\frac{i}{r^3}+\frac{1}{k_2}\frac{z}{r}\frac{1}{r^2}\right)e^{ik_1 r}, \\
B_{1\phi} &\approx \frac{\mu}{2\pi}\frac{i\cos\phi}{k_2}\frac{1}{r^3}e^{ik_2 z_s}e^{ik_1 r}, \\
r &= \sqrt{x^2+y^2+z^2}.
\end{aligned}
\tag{4.2}
$$

This approximation is valid except near the origin. For $z = 0$ the first term of $E_{1\rho}$ and $B_{1\phi}$ are the same as the lateral-wave formulas in Table 3.1, as they should be, due to the continuity of tangential fields across the sea surface. Figure 4.1 shows a comparison of true solutions $E_{1\rho}$ and $B_{1\phi}$ with those obtained from the approximations (4.1) as function of height in the air space at $x = y = 0$ right above the HED source submerged 5 m in seawater.

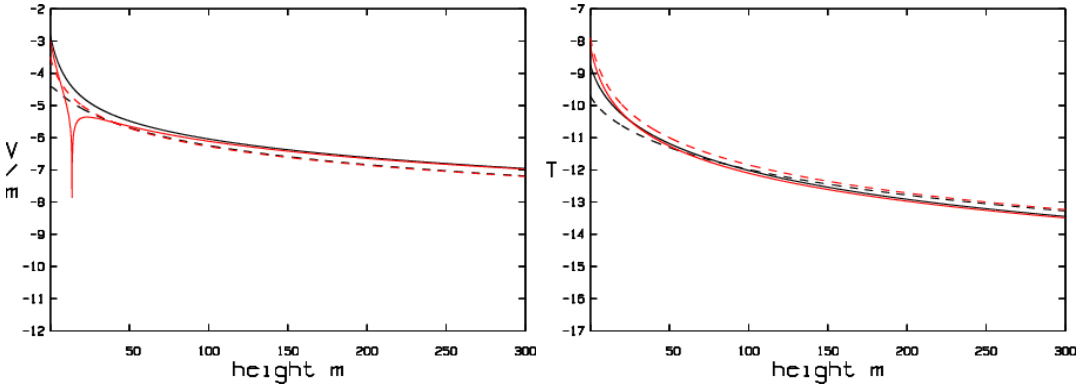

Figure 4.1: *Comparisons of the $E_{1\rho}$ (left panel) and $B_{1\phi}$ (right panel) components for ϕ=0 as function of height in the air space at $x = y = 0$. The real and and imaginary parts are plotted in solid respectively dashed lines with the exact solution in black and the approximations (4.2) in red. The source is a submerged HED at the depth 5 m and the frequency is 1 kHz. The source strength is unity and $E_{1\rho}$ and $B_{1\phi}$ are plotted in V/m respectively T in log_{10}-scale.*

Apart from a surface layer with the thickness of some 50 m, the agreement between exact and approximate solutions is excellent. We also note that the decay rate is larger for the $B_{1\phi}$ component (r^{-3}) than for $E_{1\rho}$ (r^{-2}). These curves exhibit features that are typical for the near-field of a point source in which the geometrical spread is strong close to the source while it flattens at progressively larger offsets. As opposed to a dipole field, the near-field of the air wave is radiating. For example Figure 4.2 shows flux lines of the Poynting vector in the vertical plane $y = 0$ in two cases, one with an HED source (left panel) and another one for an VMD source (right panel).

The form of the flux curves in Figure 4.2 indicates that energy is returned to the seawater, while the radiation being propagated away from the sea surface is so small that it cannot be noticed in these plots. The flux curves assumes an oval shaped path in the air, for which the height of the apex increases by propagation distance.

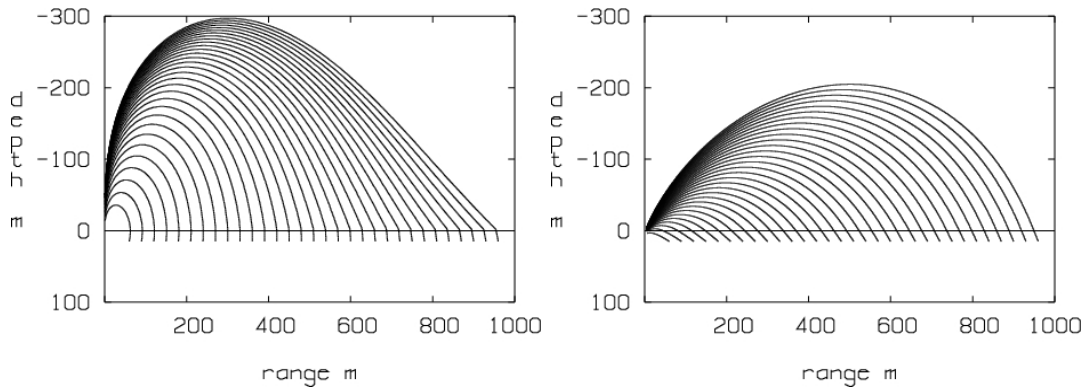

Figure 4.2: *Flux trajectories in air (locus of Poynting vector) from a submerged HED (left panel) and VMD (right panel) in the xz-plane. The source depth is 5 m and the source frequency is 1 kHz.*

5 FDTD modelling of lateral-wave propagation

The Yee scheme [7] is the most common FDTD method in computational electrodynamics. It makes use of an explicit formula to compute the electric and magnetic fields, defined on a spatial grid of points, from one time level to the next one. The update of field values takes only a few arithmetic operations at each grid point. When the Yee scheme is applied to a propagation problem in an air-sea environment the time step $\triangle t$ is subject to the stability conditions

$$\begin{aligned} \triangle t &\leq \sqrt{\mu\epsilon_1}\left(\tfrac{1}{\triangle^2 x}+\tfrac{1}{\triangle^2 y}+\tfrac{1}{\triangle^2 z}\right)^{-\frac{1}{2}}, \qquad \text{(air)} \\ \triangle t &\leq \tfrac{1}{2}\mu\sigma_2\left(\tfrac{1}{\triangle^2 x}+\tfrac{1}{\triangle^2 y}+\tfrac{1}{\triangle^2 z}\right)^{-1}, \qquad \text{(seawater).} \end{aligned} \tag{5.1}$$

where $\triangle x, \triangle y, \triangle z$ are cell sizes of a 3D grid.

The following example demonstrates the force of the constraint (5.1). For a time-harmonic source of 1 kHz an adequate spatial resolution in seawater with conductivity 0.8 S/m is $\triangle x = \triangle y = \triangle z = 4$m. Then by evaluations of the bounds (5.1) on $\triangle t$ we obtain

$$\begin{aligned} &\triangle t \leq 7.7 \cdot 10^{-6},\ \text{ms} \quad \text{(air)}, \\ &\triangle t \leq 2.7 \cdot 10^{-3},\ \text{ms} \quad \text{(seawater)}. \end{aligned} \tag{5.2}$$

If both air and seawater is included in the computational domain the smallest $\triangle t$ must be used. However the time step $7.7 \cdot 10^{-6}$ ms enforced by the propagation in air is out of proportion compared to the time scale of the source (1ms). One way to avoid computations with unphysically small time steps is to close the computational domain at the sea surface by the aid of an impedance boundary condition (IBC) that reproduces the air-sea surface effect on wave propagation in water. Such a technique was developed in [8] and later incorporated in the FDTD code [2]. The construction of the IBC was founded on the assumption of infinite speed of propagation in the air space. In the frequency domain it corresponds to setting the wavenumber of air equal

to zero. Trial computations with NLAYER in which the relative permittivity of air is is set to a very small number, say 10^{-6}, shows that this approximation is very accurate at low frequencies. The assumption of infinite speed of propagation in air implies that a disturbance that reaches the surface, instantaneously affects the field in the entire air space. Computationally the IBC leads to a system of equations for the tangential electric field at the surface. This system has to be solved in each time step. It can be done in a cost-effective way by means of a spectral decomposition of the surface field and the use of the FFT (Fast Fourier Transform) for inversion to physical space. Figure 5.1 shows a comparison of lateral-wave solutions obtained by NLAYER and and the FDTD method using IBC at the sea surface.

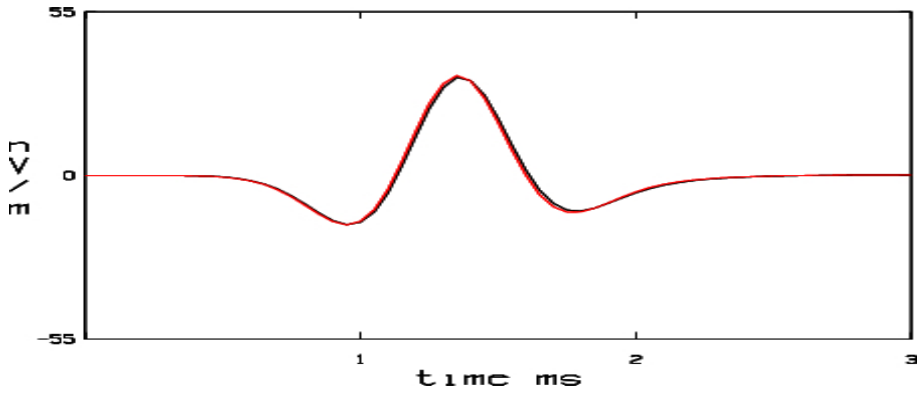

Figure 5.1: *The E_{2x} components of the exact solution (black) and the FDTD solution (red) obtained by the use of impedance boundary condition at the sea surface. The transmitted pulse is a Ricker pulse with the center frequency 1 kHz. The source and receiver depths are 5 m and the range is 150 m. The source strength is unity and the fields are shown in nV/m.*

A slight difference between the solutions in Figure 5.1 can be observed. In view of the complexity of the IBC, and discretization errors of of the Yee scheme itself, the accuracy is satisfactory.

In the presence of islands or coast lines within the computational domain it is necessary to seek an alternative approach because the design of the IBC relies on the assumption of a flat sea surface. In the following we consider the possibility of including part of the air space in the computational domain. It implies that time stepping must be performed by an implicit scheme in order to circumvent the stability constraint for an explicit scheme. Computational techniques for implicit time stepping are well known. Instead we address the problem how to confine the air space as much as possible without impeding the accuracy of the lateral wave in seawater. Even though the truncation of the air space must be done above the highest peak on land, we start to examine the case of a finite air layer above a flat surface. Figure 5.2 illustrates the impact on the field in seawater from an HED when the air space is truncated at the heights 100, 300 and 1000 m. These solutions were obtained by NLAYER using either vanishing electric (left panel) or magnetic (right panel) tangential components at the upper boundary of the truncated air layer. The impact on flux lines in air is shown in Figure 5.3 when the air space is truncated at 300 m. For a submerged VMD

the corresponding pictures are shown in Figures 5.4 and 5.5. The flux diagrams are analogous to those for half-infinite air space, which are shown in Figure 4.2.

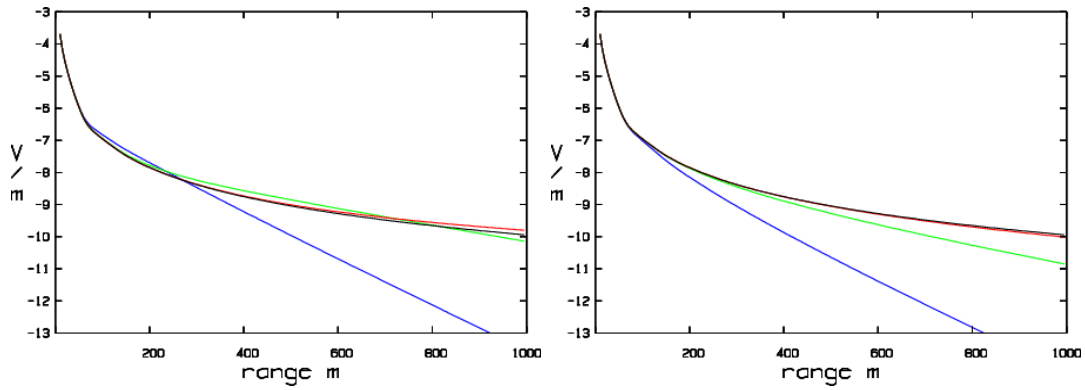

Figure 5.2: *Comparisons of the the E_{2x} component of an HED versus range for an infinite air space (black curve) and those for air spaces truncated at heights 100, 300 and 1000 m (curves in blue, green and red respectively). At the upper boundary of the air domain electric (left panel) or magnetic (right panel) tangential components are set to zero. The source and receiver depths are 5 m and the source frequency is 1 kHz. The source strength is unity and the fields are shown in V/m in in log_{10}-scale.*

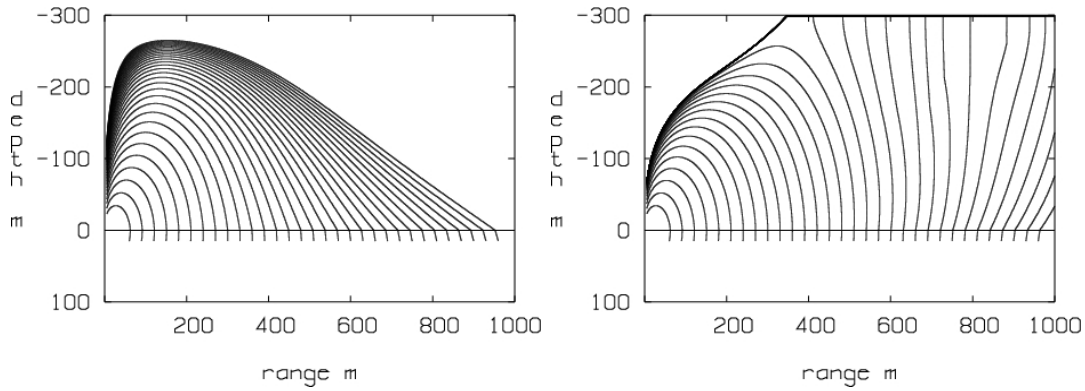

Figure 5.3: *Flux trajectories in air (locus of Poynting vector) in xz-plane from a submerged HED with electric (left) and magnetic (right) tangential components set to zero at the upper boundary of the air domain at the height 300 m. The depth of the source is 5 m and the source frequency is 1 kHz.*

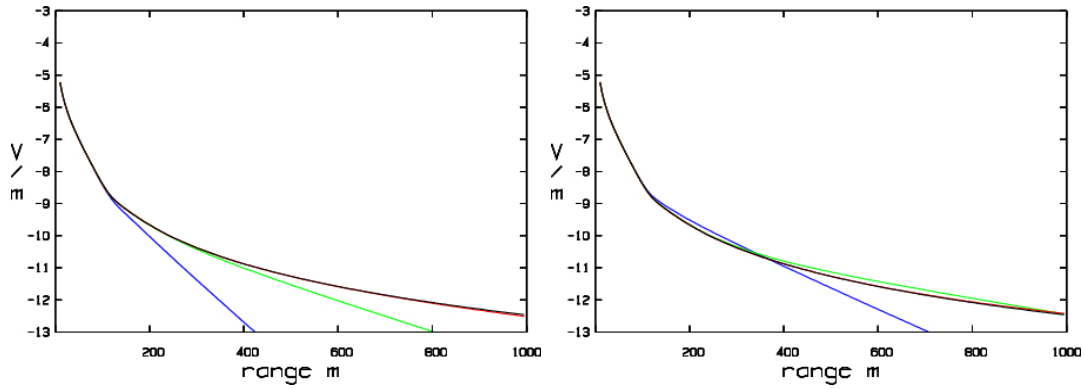

Figure 5.4: *Comparisons of the the $E_{2\phi}$ component of a VMD versus range for an infinite air space (black curve) and those for air spaces truncated at heights 100, 300 and 1000 m (curves in blue, green and red respectively). At the upper boundary of the air domain electric (left panel) or magnetic (right panel) tangential components are set to zero. The source and receiver depths are 5 m and the source frequency is 1 kHz. The source strength is unity and the fields are shown in V/m in log_{10}-scale.*

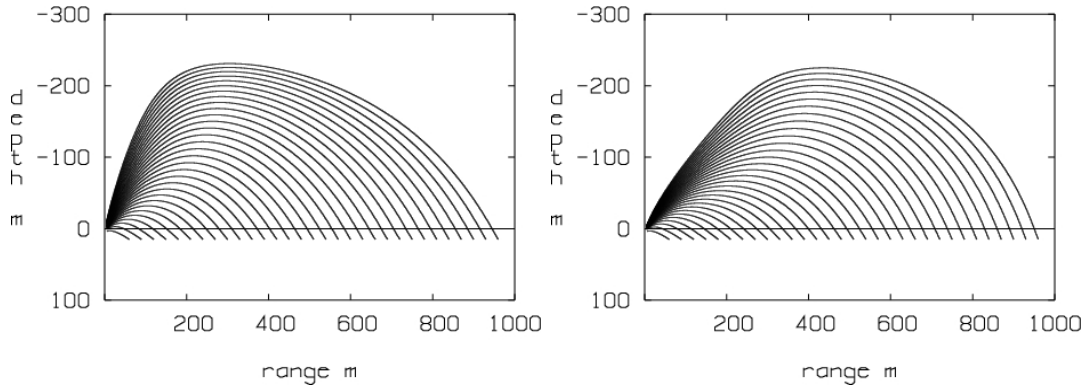

Figure 5.5: *Flux trajectories in air (locus of Poynting vector) in xz-plane from a submerged VMD with electric (left) and magnetic (right) tangential components set to zero at the upper boundary of the air domain at the height 300 m. The depth of the source is 5 m and the source frequency is 1 kHz.*

In comparing left and right panels of Figures 5.3 and 5.4 it appears preferable to close the air domain by vanishing electric components rather than magnetic ones for an HED, while the opposite case holds for the VMD. These figures indicate that it suffices to truncate the air space at a height which is comparable to the source-receiver offset. To test this hypothesis we consider a computational example of propagation of lateral waves to a distance of 150 m when the air space is truncated at the heights of 100 and 300 m. The results, which were obtained by NLAYER, are shown in Figure 5.6.

From Figure 5.6 we note that truncation at 100 m distorts the lateral wave. In addition (not shown here) a strong vertical component E_{2z} is excited, while the one for an infinite air space is very weak. The solution obtained by truncation of the air layer at the height 300 m is more accurate, although a somewhat larger air layer would be needed for a perfect match. Figure 5.7 shows the solution obtained by the FDTD

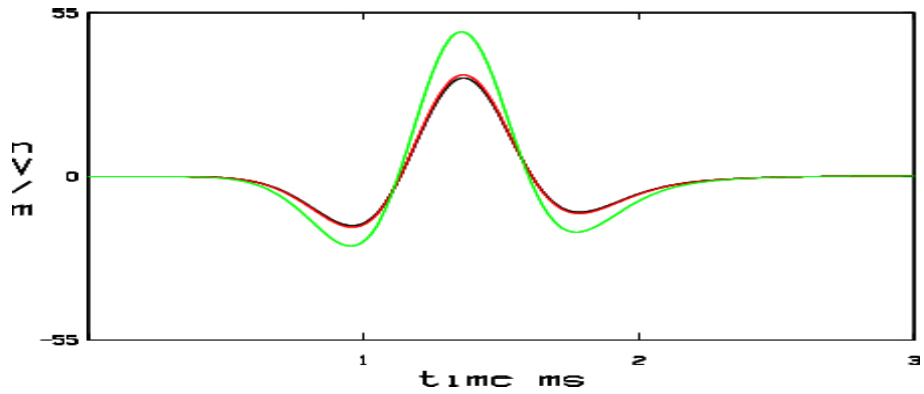

Figure 5.6: *The E_{2x} components for an infinite air space (black) and solutions with a truncated air space at the heights 100 m (green) and 300 m (red). The tangential electric components were set to zero at the upper boundary of the air layer. The transmitted pulse is a Ricker pulse with the center frequency 1 kHz from an HED. The source and receiver depths are 5 m and the range is 150 m. The source strength is unity and the fields are shown in nV/m.*

method in a domain where the air space is truncated at the height 400 m. The grid resolution in the seawater was the same as for the FDTD method with the IBC at the sea surface as shown in Figure 5.1. The accuracy of these solutions is also comparable.

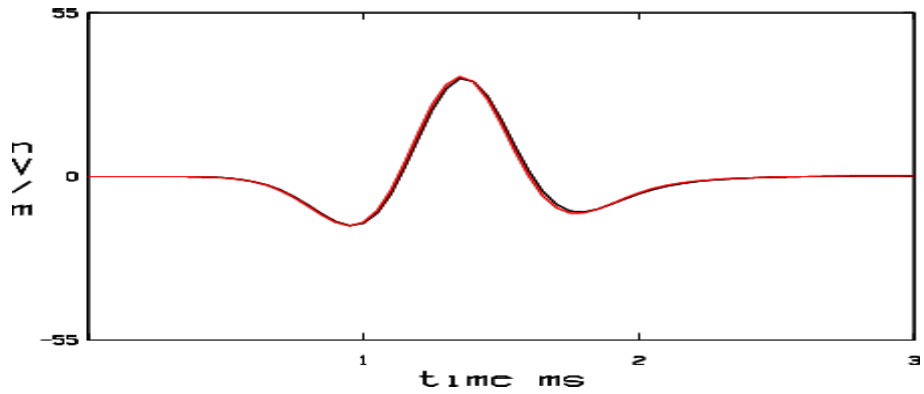

Figure 5.7: *The E_{2x} components of solutions for an infinite air space (black) and the FDTD method (red) by the inclusion of an air layer of thickness 400 m. The transmitted pulse is a Ricker pulse with the center frequency 1 kHz from an HED. The source and receiver depths are 5 m and the range is 150 m. The source strength is unity and the fields are shown in nV/m.*

5.1 Numerical examples

Here we present two computational examples of lateral-wave effects. The first one deals with the lateral wave at a rough sea surface. In the second example we consider lateral waves in the shadow of an island. Both cases are sample calculations rather than detailed expositions. The intension is to demonstrate the capability of reproducing lateral-wave effects by the finite difference method. The computations were carried

out by the FDTD program [2], which has been amended by implicit time stepping to account for an air space in the computational domain. In the following examples the number of grid cells was around 10^6 with the triple number of electric field components in the linear system of equations to be solved in each time step. The run times were around 8 h (Intel 3.2 GHz, 8 Gb memory). For problems in 3D, grid resolution is limited by available computer resources, which in turn raises concerns on accuracy of computational results. Reference cases with a flat surface were crossvalidated against NLAYER solutions. For 3D scenarios a similar check on computational results could not be accomplished due to lack of adequate validation tools. Therefore due reservations should be made regarding accuracy, although all results appear to be consistent.

5.1.1 Lateral-wave propagation over a rough sea surface

The purpose of the following example is to illustrate the effect of varying height of the sea surface on lateral-wave propagation. To begin with we take a sinusoidal surface with the amplitude 5 m and wavelength 30 m in a 2D geometry, that is the sea surface height z_h is given by

$$z_h = 5\cos\frac{2\pi x}{30}, \quad [\text{m}]. \tag{5.3}$$

with translational invariance in the y-direction. We consider transmissions from a submerged HED of Ricker pulses with the center frequency 1 kHz (skin depth 17.8 m). The source and receiver depths are 10 m, which implies that the vertical distance to the air space from an array of inline receivers varies in the range 5-15 m over a wavelength of the surface undulations. The results of this simulation is presented in Figure 5.8 for an array of seven receivers between 120 and 150 m. A notable feature

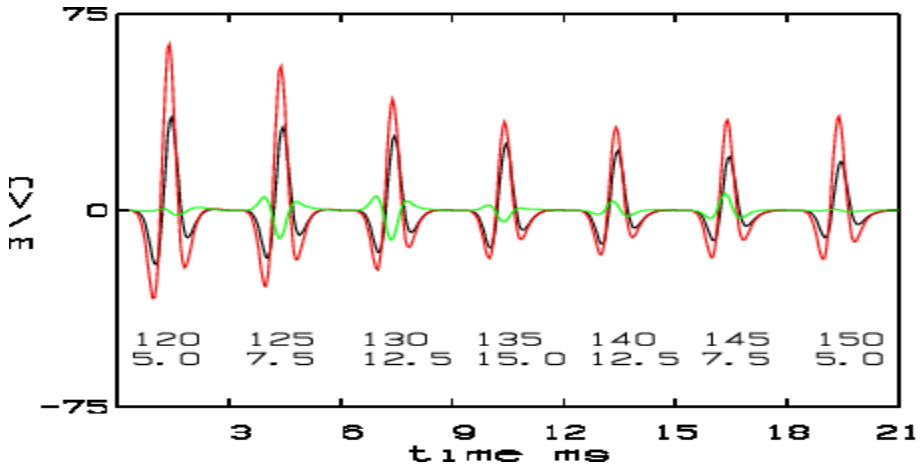

Figure 5.8: *Lateral waves induced by transmission of Ricker pulses with center frequency 1 kHz from a submerged HED. The E_{2x} components for flat (black) and sinusoidal (red) surfaces are shown at seven receivers at the ranges 120, 125,...,150 m. The range and the vertical distance from air space is marked in the figure below each arrival. The green curve is the E_{2z} component in the case of a sinusoidal surface. The source-receiver depths are 10 m.*

is that the E_{2x} component is larger with the sinusoidal surface even at ranges where

the distance to the air space is larger than the one (10 m) of the reference solution. Another feature is the strong variation of E_{2z} component, which is explained by the fact that the direction of current in the vicinity of the sea surface must conform to the tangential direction of the sea surface.

Next we consider a wind-driven sea surface described statistically according to the Pierson-Moskowitz power spectrum for a fully developed sea [9]. The analytic form of the spectrum is governed by two input parameters, the wind speed and its direction. In order to make a statistical realization of a time-varying sea surface, it is necessary to limit the frequency range by introducing a cut-off bound set to -60 dB measured with respect to the total energy of the spectrum. With this approximation, Figure 5.9 shows a sample of wave height distribution over a patch of 700×700 m^2 for a wind speed of 20 m/s in the y-direction. The peak wave height is 6.57 m, while the average height is 1.96 m. The wave height distribution in Figure is displayed at a "frozen" time of a time-varying sea surface, for which the highest frequency is 0.14 Hz. Since the time scale of the electromagnetic wave propagation problem under study is much faster (1 ms), it is reasonable to keep the sea surface profile fixed during the transmission of a Ricker pulse with the center frequency 1 kHz. A simulation was performed with the sea surface displayed in Figure 5.9 as input and with an HED source at the origin at the depth 10 m. Field points were specified on a a horizontal square $[-250, 250] \times [-250, 250]$ m at the depth 10 m.

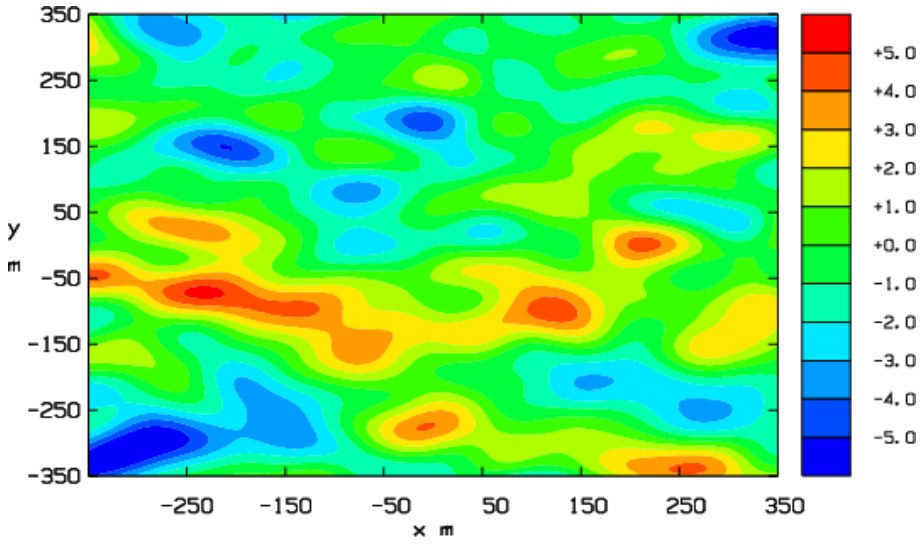

Figure 5.9: *Wave height map [m] of a Pierson-Moskowitz sea surface over a sample area of 700×700 m^2 at a "frozen" time. The wind speed is 20 m/s. The peak wave height is 6.57 m and average height is 1.96 m.*

Figure 5.10 shows the maximum horizontal electric field E_{2h} over time at each field point in a scale that compensates for expected geometrical decay of the lateral wave, that is

$$E_h = \rho^3 \max_t \sqrt{E_{2x}^2 + E_{2y}^2}. \tag{5.4}$$

Figure 5.11 shows the corresponding map of E_{2h} for a flat sea surface as obtained by NLAYER. The radial invariance of the lateral wave field when the influence of the

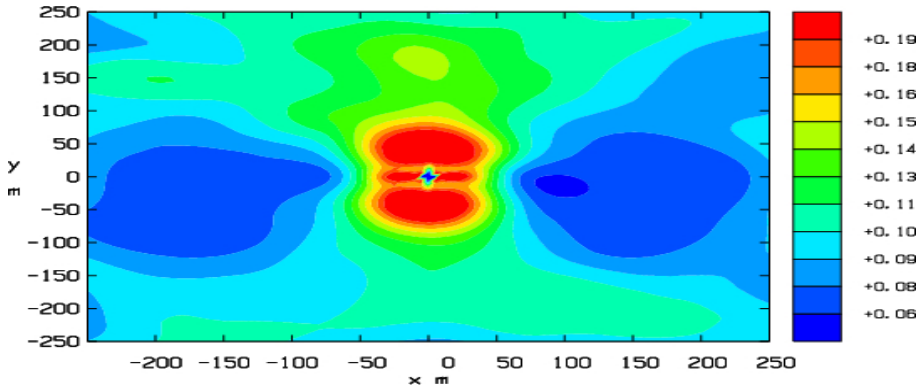

Figure 5.10: *Level map of scaled horizontal electric field E_{2h} (5.4) induced by transmission of a Ricker pulse with center frequency 1 kHz from a submerged HED in an air-sea environment with Pierson-Moskowitz sea surface as shown in Figure 5.9. The field points are located on plane at the depth of 10 m.*

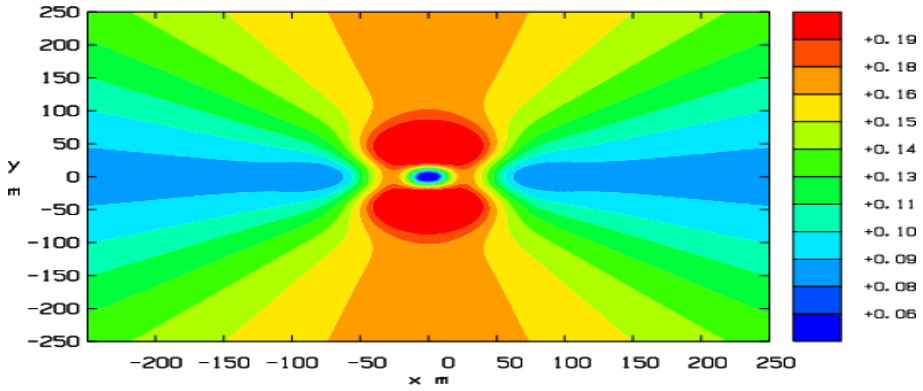

Figure 5.11: *Level map of scaled horizontal electric field E_{2h} (5.4) induced by transmission of a Ricker pulse with center frequency 1 kHz from a submerged HED in an air-sea environment with a flat sea surface. The field points are located on plane at the depth of 10 m.*

geometric factor ρ^{-3} is removed by rescaling is clearly exhibited in Figure 5.11 for the flat sea surface case. We also see that the horizontal electric field is largest in the cross line direction, which agrees with the observation in Table 3.1 that $E^L_{2\rho}$ and $E^L_{2\phi}$ differs by a factor of two albeit different azimuthal dependence. On the whole the radial structure of the field is present also in the rough sea surface case as displayed in Figure 5.10, although local deviations from the flat sea surface case may amount to double magnitudes of field values. In the rough sea surface case the E_{2z} component is excited and comparable in magnitude with the horizontal field. Nevertheless the above sample calculations provide evidence for the hypothesis the both range of propagation and geometrical decay of the lateral wave in the presence of a rough sea surface is about the same as for a flat sea surface.

5.1.2 Lateral-wave propagation across a rocky island

The purpose of the following example is to see whether the presence of an island has a shadowing effect on the lateral wave. We consider two cases in which the island at the sea surface assumes the form of a circle of diameter 50 m and another case with an elliptic cross section with diameters 50 and 200 m in the x- and y-directions respectively. The center of the island has the coordinates (100,0) m. The protrusion above the sea surface is taken as a circular or elliptic paraboloid with a peak height of 10 m. The subsurface shape is taken as a cylinder with the same cross section as in the sea surface, that is the boundary of the island is vertical in the water volume. In terms of an anomalous conductivity σ_a in a layered background of half-infinite spaces of air and seawater the island is defined by

$$\begin{aligned}
&\text{for } z < 0 \quad \text{(air)}: \quad \sigma_a = 0.001 \text{ S/m}, \text{ if } E(x,y) \le 0 \text{ and } z > E(x,y),\\
&\text{for } z \ge 0 \quad \text{(seawater)}: \quad \sigma_a = 0.001 \text{ S/m}, \text{ if } E(x,y) \le 0,\\
&\text{where } E(x,y) = \frac{(x-100)^2}{a} + \frac{y^2}{b} - 10, \quad \begin{cases} a = b = 62.5, & \text{circular shape,} \\ a = 62.5, b = 1000, & \text{elliptic shape.} \end{cases}
\end{aligned} \tag{5.5}$$

The HED source is located at (0,0,5) m and an array of inline receivers at the same depth are placed on the shadow side of the island, which ends at x=125 m, from 130 m to 160 m in steps of 5 m. Figure 5.12 and 5.13 show E_{2x} and E_{2z} components at the seven receivers for transmission of Ricker pulses with the center frequency 1 kHz.

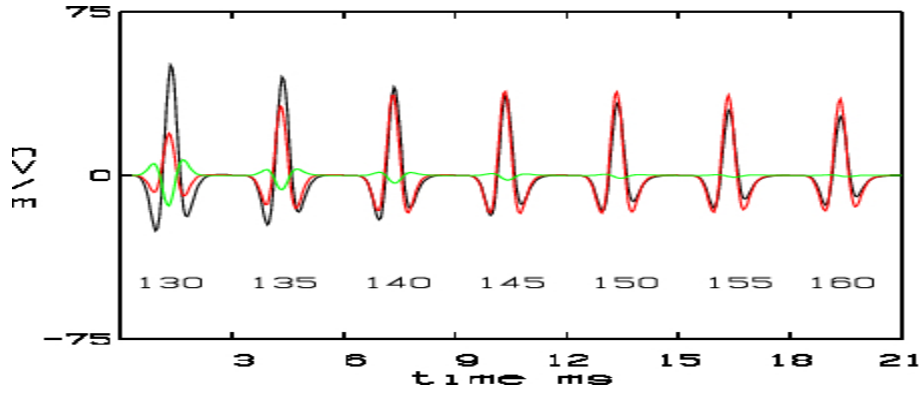

Figure 5.12: *Lateral waves induced by transmission of Ricker pulses with center frequency 1 kHz from a submerged HED in an air-seawater environment with an island in the form a circle with the diameter 50 m and its center at (100,0,0) m. The E_{2x} components for a flat surface (black) and with the island present (red) are depicted at seven inline field points behind the island (labeled by source-receiver range in the figure). The green curve is the E_{2z} component in the case with the island present. The source-receiver depths are 5 m.*

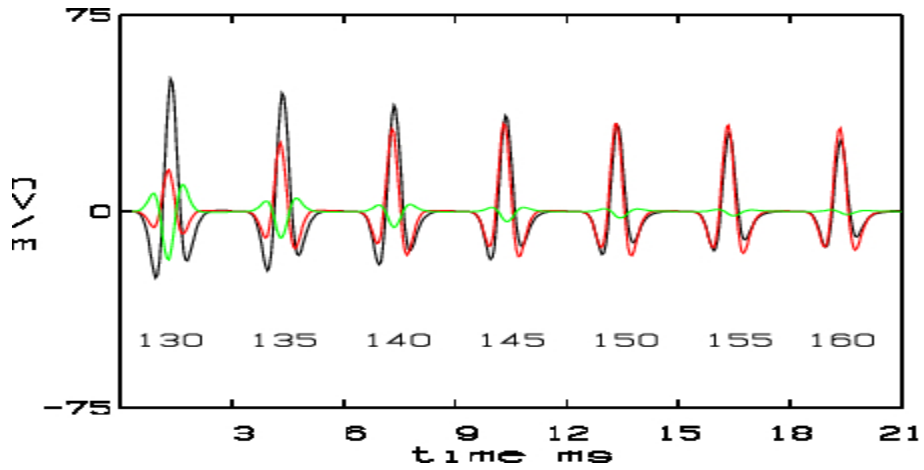

Figure 5.13: *Lateral waves induced by transmission of Ricker pulses with center frequency 1 kHz from a submerged HED in an air-seawater environment with an island in the form an ellipse. The diameters of the ellipse are 50 m (inline) and 200 m (transverse) and its center is (100,0,0) m. The E_{2x} components for a flat surface (black) and with the island present (red) are depicted at seven inline field points behind the island (labeled by source-receiver range in the figure). The green curve is the E_{2z} component in the case with the island present. The source-receiver depths are 5 m.*

As can be observed in Figures 5.12 and 5.13, the response is limited to the first few receivers at distances of 5, 10, and 15 m from the island. The impact of enlarging the transverse dimension of the island from 50 to 200 m is modest. The interpretation of the lateral-wave effect is complicated by the high resistivity of the island, which promotes transmission by paths within the body of the island. To assess this effect a complementary run was made with the conductivity of the island set to σ_a= 10 S/m, which at the frequency 1 kHz obstructs transmission through the body of the island. This change of conductivity resulted in lateral wave components that were almost the same as in the flat surface case even at the receiver with the closest offset of 5 m to the island. Therefore the distortion seen at receivers in the close vicinity of the resistive island appear to be caused by interference of two contributions, the lateral wave and radiation from an excited field within the island.

6 Conclusions

Summarizing this report, we have reviewed basic features of the lateral wave at the air-sea surface in the case of subsurface-to-subsurface propagation at low frequencies ($<$ 300 kHz). This survey was guided by the aim to pinpoint characteristics that are critical to the development of computational models, in particular FDTD and FDFD methods, which are capable of reproducing air-sea surface effects with good fidelity. In the important case that part of the air space is included in the computational domain, the results of this report indicate that the air layer must be sufficiently large but not excessively large. Coarsely, domain truncation of the air space can be made at a height equal to the triple of the source-receiver offset. A more precise determination can be

produced by trial calculations by the NLAYER program at a modest computational effort. These prior calculations should be automatized and incorporated as part of a FDTD (or FDFD) program for low frequency modelling of electromagnetic propagation in air-sea environments.

In the course of this work new questions have arisen concerning lateral wave effects in the presence of a wavy sea surface and islands. A few sample calculations indicate that the lateral wave is a strong and persistent feature which is only slightly affected by deviations from an ideally flat sea surface. Further insights into this phenomenon could be pursued using an interplay between physics, mathematical and numerical modelling.

References

[1] L. Abrahamsson and B.L. Andersson. NLAYER: an ELFE code for horizontally stratified media. Technical report FOA-R–97-00586-409–SE, 1997.

[2] L. Abrahamsson. An FDTD method for ELFE propagation in seawater. Technical report FOA-R–00-01735-409–SE, 2000.

[3] A.C. Fraser-Smith, A.S. Inan, O.G. Villard Jr., and R.G. Joiner. Seabed propagation of ULF/ELF electromagnetic fields from harmonic dipole sources located on the seafloor. *Radio Sci.*, 23:931–943, 1988.

[4] J.I. Nordskag and L. Amundsen. Asymptotic airwave modeling for marine controlled-source electromagnetic surveying. *Geophysics*, 72:F249–F255, 2007.

[5] D. Andréis and L. MacGregor. Controlled-source electromagnetic sounding in shallow water: Principles and applications. *Geophysics*, 73:F21–F32, 2008.

[6] R.W.P. King, M. Owens, and T.T. Wu. *Lateral Electromagnetic Waves*. Springer-Verlag, 1992.

[7] K.S. Yee. Numerical solution of initial boundary value problems involving Maxwell's equations in isotropic media. *IEEE Trans. Antennas and Propagation*, 14:302–307, 1966.

[8] S. Johansson. Domain truncation in the time-domain finite-difference method for Maxwell's equations in seawater. Methodology report FOI-R–0090-SE, 2001.

[9] L. Fortuin and J.G. de Boer. Spatial and Temporal Correlation of the Sea Surface. *J. Acoust. Soc. Amer.*, 49:1677–1679, 1971.